Chapter 14

Electron step-size artefacts and PRESTA

In the first half of this chapter we shall discuss electron step-size artefacts, the reasons for calculation of spurious results under some circumstances, and simple ways by which these calculational anomalies may be avoided. In the second half of the chapter, we shall discuss a more sophisticated electron transport algorithm, called PRESTA, which solves this problem of step-size dependence in most cases.

The chapter will proceed within the context of the EGS4 code [NHR85] although the ideas put forth apply to all electron transport codes which use condensed-history methods. Calculations which signal the existence of step-size anomalies will be presented along with the improvements to the electron transport algorithm which were used to circumvent the problem.

14.1 Electron step-size artefacts

14.1.1 What is an electron step-size artefact?

An electron step-size artefact is characterized by the dependence of some calculated result upon arbitrary "non-physics" parameters of the electron transport. This is illustrated by the example given in fig. 16.1. In this example, 1 MeV electrons were incident normally upon a $3r_0/2$ thick slab of water. The quantity r_0 is the range calculated in the continuous-slowing-down approximation (CSDA). The energy deposited between $r_0/2$ and r_0 was scored. Two ways of calculating the energy deposition are depicted. The first, (EGS (with PLC), lower dashed line) is the default EGS calculation. "PLC" stands for path-length correction, which includes the effect of electron path curvature for each electron step. The second, (EGS (no

Figure 14.1: The relative energy deposit from 1 MeV electrons incident normally on a $3r_0/2$ slab of water. The energy deposited between $r_0/2$ and r_0 is shown. The upper dashed line is an EGS calculation without the electron step-size shortened by ESTEPE and without path-length corrections (PLC's). The lower dashed line is an EGS calculation without ESTEPE control and including the default PLC employed by EGS.

PLC), upper dashed line) neglects this correction. Rogers [Rog84b] added an electron step-size limit, ESTEPE, the maximum allowable fractional kinetic energy loss per electron step to "continuous" energy-loss processes in order to obtain better agreement in the low-energy region. One notices a dramatic increase in the "with PLC" curve with smaller ESTEPE and a commensurate decrease in the "no PLC" curve. Why should a calculated result depend so strongly on an arbitrary parameter such as electron step-size unless some basic constraints of the underlying theory are being violated? What is the role of path-length corrections? Does the electron transport algorithm have enough physics' content to accurately simulate electron transport? An even more important question is "*What is the correct answer?*". (If a correct answer is to be obtained for a case that exhibits step-size dependence, it is always found at smaller step-sizes within certain constraints that we shall discuss later.)

As another example of dramatic step-size effects, consider the irradiation geometry depicted in fig. 16.2. In this case, a 1 MeV zero-area beam of electrons was incident on the center

Figure 14.2: The irradiation geometry of the "thin tube" simulation. A zero-area beam of 1 MeV electrons was incident on the center of the end of a 2 mm diameter, 20 cm long tube of air.

of the end of an air tube which was 2 mm in diameter and 20 cm long. The results are plotted in fig. 16.3. The dose deposited in the air cylinder was scored as a function of SMAX, the maximum geometrical step-length allowed. This parameter was also introduced by Rogers [Rog84b] in adapting the EGS code to low-energy simulations. The default EGS simulation (equivalent to setting SMAX = 20 cm, the length of the tube) is wrong since most often the electrons only take one step through the tube, as depicted in fig. 16.4. All the "continuous" energy deposition associated with this step is deposited within the air tube resulting in too high a value being calculated. Reducing SMAX to 10 cm, half the length of the tube, almost halves the energy deposition, as seen in fig. 16.3. In this case, most of the electrons that are transported 10 cm immediately scatter out of the tube, as depicted in fig. 16.5. Further reduction of SMAX reduces the energy deposited to the tube as the electron transport simulation becomes more and more accurate. Finally, a flat region of "convergence" is obtained in the vicinity of 0.2 to 1.0 cm, a scale of magnitude comparable to the diameter of the tube. As seen in fig. 14.6, the small transport steps allow the electron to escape the tube or be transported down it, in accord with the random selection of the

Figure 14.3: The relative dose deposited in the air cylinder is plotted as a function of SMAX. In the "default EGS" case, the electrons are usually transported the length of the tube resulting in an anomalously high calculated dose to the tube.

Figure 14.4: In the default EGS calculation the electrons most often travel the length of the tube. Note that the vertical scale in this and the next two figures is greatly exaggerated. The tube is actually 2 mm in diameter and 20 cm long. The $\times$'s mark the end-points of each electron step.

Figure 14.5: If SMAX is reduced to 10 cm, half the length of the tube, then the electrons that are transported 10 cm usually scatter out of the tube immediately.

multiple scattering angle for each step. In this region, the transport is being simulated more

Figure 14.6: When the transport steps are shortened to a length comparable to the diameter of the tube, the electron may or may not scatter out of the tube, obeying the probabilistic laws of multiple scattering.

or less accurately.

At step-sizes in the vicinity of 1 mm and smaller we observe another artefact in fig. 16.3. We again notice anomalously high results. The reason for the occurrence of this artefact has to do with the minimum step-size that can be accommodated by the multiple scattering formalism used by the EGS code. (EGS uses the Molière formalism [Mol47, Mol48] as expressed by Bethe [Bet53].) At these smaller step-sizes multiple scattering formalism should be replaced by a "few-scattering" or "single-scattering" formalism. EGS does not do this but rather "switches off" the multiple scattering formalism and no elastic electron-electron or electron-nucleus scattering is modelled. Once more the electrons are transported in straight lines down the length of the tube. We must, therefore, qualify a statement expressed earlier in the chapter. If a correct answer is to be obtained with the EGS code for a case that exhibits a step-size dependence, it is obtained by using small step-sizes with the proviso that the multiple scattering is not "switched off" for a substantial number of the electron transport steps. The various limits on transport step-size will be discussed in more detail later in the chapter.

The previous example was contrived to show large changes in calculated results with step-size. It represents the extreme limit of what the EGS code is capable of. As a final example we show a large step-size dependence for a case where the electrons are almost in a state of equi-

librium. This is the case of a thick-walled ion chamber exposed to ^{60}Co photons. We show, in fig. 14.7, the variation with ESTEPE of the calculated response of a 0.5 g/cm^2 carbon-walled

Figure 14.7: Calculated response of a thick-walled carbon chamber (0.5 g/cm^2 carbon walls, 2 cm diameter, 2 mm thick cylindrical air cavity), exposed to 1.25 MeV photons incident normally on a flat circular end.

ion chamber with a cylindrical air cavity 2 mm in depth and 2 cm in diameter exposed to a monoenergetic beam of 1.25 MeV photons incident normally upon one of the flat ends. The results are normalized to the theoretical predictions of Spencer-Attix theory [SA55] corrected for photon attenuation, photon scatter and electron drift affects [BRN85, RBN85]. According to the theorem of Fano [Fan54], the electron fluence in the chamber in the vicinity of the cavity is almost unperturbed by the presence of the cavity in this situation. (Strictly speaking, Fano's theorem only applies to density changes in one medium. However, carbon and air are not too dissimilar except for their densities and Fano's theorem may be applied with negligible error.) The electrons in this simulation are almost in complete equilibrium. Non-equilibrium effects requiring corrections to Spencer-Attix theory amount to only a few percent of the total response. Why then, should the electron step-size play such a critical role in a simulation where electron transport does not matter a great deal to the physics? We observe, in fig. 14.7 a step-size variation of about 40% when ESTEPE is changed from 1% to 20%! To answer this question requires some closer examination of the various elements of electron transport.

14.1.2 Path-length correction

To illustrate the concept of path-length correction, we consider the example of 10 MeV electrons incident normally upon a 1 cm slab of water. The top curve in fig. 14.8 depicts

Figure 14.8: A 10 MeV electron being transported through a 1 cm slab of water as simulated by EGS in its default configuration (no ESTEPE or SMAX control, note that the electron takes only one step to cross the water slab) and with an ESTEPE of 10, 5, 2, and 1%.

a typical EGS electron transport step through this slab with the EGS system used in its default configuration (no ESTEPE or SMAX control). Note that the electron went through in only one step. The other curves in fig. 14.8 depict similar histories except that ESTEPE has been adjusted to 10, 5, 2, or 1%. As ESTEPE gets smaller and smaller, the electron tracks begin to "look" like real electron tracks, similar to those that one would observe, for example, in bubble chamber photographs. We know that electron steps are curved, as depicted in the previous figures. Must we use exceedingly small electron steps to calculate accurately in Monte Carlo simulations? The answer depends upon the application. If one is interested in accurate physical "pictures" of electron tracks, then short step-sizes, consistent with the resolution desired, must be used. However, imagine that we are only interested in calculating the energy deposited in this slab. Then, considering fig. 14.8 with the realization that the energy deposited is proportional to the total curved path, it would be possible to simulate passage through this slab using only one step *if one could accurately correct for the actual path-length the electron would have travelled if one had used very small steps.*

Figure 14.9 depicts the relationship between the total curved path of a step and its straight-line path in the direction of motion at the start of the step. For a given value of the curved

Figure 14.9: A pictorial representation of the total curved path-length of an electron step, t, and the straight-line path-length, s, in the direction of motion at the beginning of the step. The average lateral deflection of a transport step, ρ, is related to t. The displacements s and ρ are mutually orthogonal.

path-length, t, the average straight-line path in the starting direction of motion, s, are related by eq. 17.1 which has been attributed to Lewis [Lew50],

$$s = \int_0^t dt' \langle cos\Theta(t') \rangle, \tag{14.1}$$

where $\Theta(t')$ is the multiple scattering angle as a function of the actual curved path-length along the path, t', and the average value, $\langle\rangle$, is to be computed using the probability distribution of any multiple scattering theory. Several strategies have been developed for calculating s using the Lewis equation. Yang [Yan51] advocated an expansion of eq. 17.1 to second order in Θ and the use of a small-angle multiple scattering theory to compute the average value. This is the strategy employed in the EGS code where the Fermi-Eyges multiple scattering theory [Eyg48] is used to compute the average value. (As mentioned previously, the multiple scattering in EGS is performed using Bethe's formulation of the Molière theory.) Unfortunately, this approach has been shown to produce path-length corrections, $(t-s)/s$, a factor of 2 too high [HW55, BR87]. Berger [Ber63] advocated the relation,

$$s = \frac{1}{2} t[1 + \cos(\Theta(t))], \tag{14.2}$$

and he showed that s calculated using this equation agrees with that calculated using eq. 17.1 in the limit of small angle if the multiple scattering theory of Goudsmit and Saunderson [GS40a, GS40b] is used. Bielajew and Rogers [BR87] expanded eq. 17.1 to 4^{th} order in Θ and evaluated the average value using Bethe's version of Molière's multiple scattering theory. They showed that this approach and s calculated using eq. 17.3 agree, even for large average scattering angles of the order of a radian. The proof that this approach is valid is given later in the chapter.

The path-length correction can be quite large, as seen in fig. 14.10, where the path-length correction, $(t-s)/s$, in water is plotted versus electron kinetic energy for various step-sizes as measured by ESTEPE. If one wishes to reduce computing time by using large electron

Figure 14.10: The path-length correction in water versus kinetic energy for various step-sizes as measured by ESTEPE. The line $t = t_{max}$ shows the maximum step-size allowed by the Molière theory.

steps, then one must correct for path-length curvature. The larger the step, the greater the correction. Greater corrections are needed for lower energies as well. Recall that the path-length correction used by EGS is about a factor of 2 too high. This fact is almost entirely responsible for the step-size artefact seen in fig. 16.1. Too much curvature correction resulted in too much energy being deposited in the first $r_0/2$ slab and, by conservation of energy, too little in the second. In the "no PLC" case, the opposite prevailed. The *failure* to account for electron path-length curvature leads to less energy deposition in the upstream slab and too much in the downstream one. As the step-size is reduced, however, the electron tracks are modelled more and more correctly, relying on multiple scattering selected for each of the steps for the development of curvature of the tracks. If one uses a correct path-length correction, such as that proposed by Berger [Ber63] or Bielajew and Rogers [BR87], then most of the step-size artefact vanishes, as exhibited in fig. 14.11. The residual step-size

Figure 14.11: The deep energy deposition problem described for fig. 16.1. In this case, a "proper" (*i.e.* demonstrably correct) path-length correction is used to eliminate most of the step-size dependence.

dependence has to do with other neglected features of electron transport that we have yet to discuss.

We now return to the ion chamber simulation and see what effect the use of a correct path-length correction has. Figure 14.12 shows the improvement of the ion chamber calculation, a reduction in the step-size dependence with use of a proper path-length correction. Yet, there still remains a considerable dependence on ESTEPE. Some physics must be missing

Figure 14.12: The ion chamber calculation described for fig. 14.7 with a reduction of the step-size dependence with the use of a "proper" path-length correction. A significant step-size dependence remains.

from this simulation!

14.1.3 Lateral deflection

Returning to fig. 14.8, we see that as the step-size is made smaller and the electron histories are simulated with increasing accuracy, not only does the electron path acquire curvature, it is also deflected laterally. If one is faced with a simulation in which lateral transport is important (for example, the air tube of figs. 16.2 and 16.3), but one wishes to use as few electron steps as possible, one ought to account for the the lateral deflection *during the course of each electron step*. If we use a sufficiently small step-size, this lateral deflection will occur naturally as the multiple scattering angle selected for each electron step deflects the electron, accomplishing the lateral transport. We saw that in the example of the air tube, if the step-size was restricted to be of the order of the diameter of the tube, the effects of lateral transport were incorporated properly in the simulation. Therefore, if one wishes to use fewer transport steps in a simulation of this nature, a more sophisticated approach is needed.

Figure 14.9 illustrates the basic concept of the lateral deflection. An average lateral deflection, ρ, is associated with an electron transport step characterized by the total curved path of the step, t. Berger [Ber63] has provided a method that correlates ρ with t and the multiple scattering angle, Θ, for the electron step,

$$\rho = \frac{1}{2} t \sin \Theta(t). \tag{14.3}$$

This is called the "lateral correlation" because the displacement, ρ, is correlated to the multiple scattering angle [Ber63]. The proof that this prescription is valid will be given later. Figure 14.13 shows that this correction is large for large step-sizes and small energies. We shall show, in another section, evidence of the reduction of step-size artefacts through the use of Berger's lateral correlation algorithm.

14.1.4 Boundary crossing

A general Monte Carlo method should be able to simulate electron trajectories in complex geometries. The condensed-history technique, whether the multiple scattering is performed through the use of the theories of Fermi-Eyges, Molière, or Goudsmit-Saunderson, is limited by the fundamental constraints of these theories. These theories are strictly applicable in only infinite or semi-infinite geometries. Some theories (*e.g.* Fermi-Eyges, Molière) are applicable only for small average scattering angles as well. It would be far too complex to construct a multiple scattering theory that applies for all useful geometries. In particular, how should a Monte Carlo electron transport algorithm treat the approach and retreat from

Figure 14.13: The average angular correlation versus electron kinetic energy for various step-sizes as measured by ESTEPE. The reader is referred to ref. [BR87] for the calculational details used in the construction of this figure.

arbitrarily shaped boundaries yet still not violate the basic constraints of the underlying theories? Unless multiple scattering theories become much more sophisticated, there is only one solution — *shorten the electron steps in the vicinity of boundaries so that for a majority of electron steps in the simulation, any part of the total curved path is restricted to a single medium.* In other words, the underlying theories rely upon the particle transport taking place in an infinite, or semi-infinite medium. Therefore, in the vicinity of a boundary, the electron step should be shortened enough so that the underlying theory is not violated, at least for most of the transport steps. The details of how this boundary crossing is accomplished is very much code-dependent. However, the above "law" should apply for all condensed-history Monte Carlo methods. The details of how this can be accomplished with the EGS code will be given later.

14.2 PRESTA

14.2.1 The elements of PRESTA

So far we have discussed electron step-size artefacts and how they can be circumvented by shortening the electron transport step-size. The occurrences of artefacts were related to a shortcoming in, or the lack of, a path-length correction, the lack of lateral transport during the course of an electron step, or the abuse of the basic constraints of the multiple scattering theory in the vicinity of boundaries describing the geometry of the simulation. PRESTA, the Parameter Reduced Electron-Step Transport Algorithm [BR87], attempts to address these shortcomings with the EGS code. The general features of PRESTA are applicable to all condensed-history codes. The fine details, only a few of which we shall discuss, are not. Before plunging ourselves into the features of PRESTA, we return to the examples dealt with earlier in the chapter and show how PRESTA handles the difficulties.

We have discussed the energy deposition in the middle of three $r_0/2$ slabs due to 1 MeV electrons. Recall that in fig. 16.1 we saw large step-size artefacts produced by the EGS code that could be "healed" by using short step-sizes. Later in fig. 14.11 we cured most of the problem by using a correct path-length correction. In fig. 14.14, we also include lateral deflections and a careful boundary crossing algorithm, (the remaining components of PRESTA), and all residual variation with step-size disappear. In this example, it was the correct path-length correction which was responsible for most of the improvement. The correct path-length correction method is one of the major components of PRESTA.

In the ion chamber simulation of figs. 14.7 and 14.12, the improvement of ion chamber response was quite dramatic but still incomplete. The evidence of step-size dependence was still quite strong. Once PRESTA is used for the simulation, however, the step-size artefact vanishes, as evidenced in fig. 14.15. It is the inclusion of lateral transport that is responsible for the remaining improvement in this case.

Figure 14.14: The energy deposition to the middle of three $r_0/2$ water slabs due to 1 MeV electrons. This simulation was discussed previously in figs. 16.1 and 14.11. When PRESTA is used, all evidence of step-size dependence vanishes.

Figure 14.15: The ion chamber response calculation visited already in figs. 14.7 and 14.12. The use of PRESTA virtually eliminates any step-size dependence in this calculation.

Finally, the improvement in the air tube calculation of fig. 16.3 is shown in fig. 14.16. In this case, it is the boundary crossing algorithm that is almost entirely responsible for the improvement.

Therefore, path-length correction, lateral deflection and a careful boundary crossing algorithm are essential elements of a general purpose, accurate electron transport algorithm. It remains to be proven in a more rigorous fashion that these components are physically valid in a more general context other than the examples given. Otherwise the improvements may be fortuitous. To do this requires a brief introduction to the Molière theory, specifically on the limits on electron step-size demanded by this multiple scattering formalism.

14.2.2 Constraints of the Molière Theory

In this section we briefly discuss the physical constraints of the Molière multiple scattering theory. Rather than present many mathematical formulae, we concentrate on graphical representations of the various limits. For further detail, the reader is encouraged to examine refs. [NHR85, BR87] for the implementation of the Molière theory in the EGS code. The original papers are enlightening [Mol47, Mol48], and the exposition of Molière's theory by Bethe [Bet53] is a true classic of scientific literature.

Figure 14.16: The air tube calculation of fig. 16.3 is dramatically improved by the use of PRESTA. The label blcmin= 1.989 refers to a parameter that controls the boundary crossing algorithm. This point is discussed later.

The Molière theory is constrained by the following limits:

- The angular deflection is "small". (The Molière theory is couched in a small angle approximation.) Effectively, this constraint provides the upper limit on step-size.
- The theory is a *multiple* scattering theory, that is, many atomic collision participate to cause the electron to be deflected. Effectively, this constraint provides the lower limit on step-size.
- The theory applies only in infinite or semi-infinite homogeneous media. This constraint provides the motivation for treating the electron transport very carefully in the vicinity of interfaces.
- Energy loss is not built into the theory.

Bethe [Bet53] carefully compared the multiple scattering theories of Molière [Mol47, Mol48] and Goudsmit-Saunderson [GS40a, GS40b]. The latter theory does not resort to any small-angle approximation. Bethe showed that the small angle constraint of the Molière theory can be expressed as an equation that yields the maximum step-size [NHR85, BR87]. Below this limit, the two theories are fundamentally the same. This upper limit is used by PRESTA. (The default EGS upper limit is actually about 0.8 of the PRESTA limit.) Bethe's upper limit is plotted in fig. 14.17 as the curve labelled t_{max}. Also plotted in this figure is the CSDA range [BS83]. We note that at larger energies, greater than about 3 MeV in water, the CSDA range is a more stringent restriction on electron step-size. This means that for large energies, step-sizes can be quite large, up to the range of the electron. However, one must recall that the Molière theory does not incorporate energy loss directly. Therefore, if we wish to approach the upper limit on step-size, we must treat the energy loss part of the problem carefully. This topic will be discussed in a later section.

There is a critical parameter in the Molière theory, Ω_0, that can be interpreted as the number of atoms that participate in the multiple scattering. Molière considered his development to be valid for $\Omega_0 \geq 20$. It has been found that sensible results can be obtained for $\Omega_0 \geq e$ [BR87]. The lower limit, $\Omega_0 = e$, represents the "mathematical" limit below which Molière's formalism breaks down mathematically. It is interesting that Molière's theory can be "pushed" into the "few-scattering" regime and still produce reliable answers. We shall return to this point later. The minimum step-size, t_{min}, obeying $\Omega_0 = e$ is plotted versus electron kinetic energy in fig. 14.17 for water. We see in this figure, that the minimum and maximum step-sizes are the same at about 230 eV in water. Therefore, this represents the absolute minimum energy for which multiple scattering can be modelled using the Molière theory. (In this energy region, atomic binding effects begin to play an increasingly important role requiring the use of more sophisticated low-energy theories.) As the energy increases, so does the range over which the Molière theory is valid. The lower limit reaches an asymptotic bound at about 4×10^{-4} cm, while the upper limit continues upwards monotonically with

Figure 14.17: The minimum and maximum step-size limits of the Molière theory, t_{min} and t_{max} respectively. These limits are for water and the behavior for other materials can be obtained elsewhere [NHR85, BR87]. The dashed curve is the CSDA range [BS83].

increasing energy. Thus, for high energy, the applicable range in water extends from about 4 microns to the electron CSDA range.

In a previous section we discussed a type of artefact that can be problematic with the EGS code. That is, if one demands a step-size that is too short, EGS "turns off" the simulation of multiple scattering. We saw a dramatic example of this in fig. 16.3. Figure 14.18 compares

Figure 14.18: Electron step-size is plotted versus kinetic energy for various values of ESTEPE and t_{min}. These curves apply for water. For other media, consult ref. [NHR85, BR87]. If one demands a 0.1% ESTEPE in water, then multiple scattering cannot be modelled using the Molière theory for electrons below about 500 keV.

t_{min} with step-sizes measured by various values of ESTEPE as calculated for water. Note that if one demands a step-size of 1% ESTEPE, then multiple scattering will not be simulated for electrons with energies less than about 40 keV. To circumvent this problem, PRESTA does not allow the ESTEPE restriction to reduce step-size below t_{min}.

The answer to the question, "Is the Molière theory valid between these upper and lower limits?", is a complicated one. The benchmarking of PRESTA can be construed as a verification of the consistency of the Molière theory. If the Molière theory contained any intrinsic step-size dependence, then so would the results calculated using PRESTA, barring some highly fortuitous coincidences. In the next few subsections, we examine all the components of PRESTA, trying the utmost to omit unnecessary complications.

14.2.3 PRESTA's path-length correction

In section 14.1.2 we discussed a new path-length correction. This method used the Lewis formula, eq. 17.1, expanded it to 4^{th} order in Θ, and evaluated the mean values using the Molière distribution functions [BR87]. We have seen impressive reductions in step-size dependences exhibited in figs. 14.11 and 14.12. It now remains to prove that this path-length correction is valid in more general applications. To this end, we modify our electron transport algorithm in the following fashion to conform with all the constraints of the Molière theory:

- Energy loss mechanisms are "switched off", including losses to "continuous" and "discrete" processes.
- Bounding surfaces of all kinds are eliminated from the simulations. The transport takes place in an infinite medium.
- The step-size constraints of the Molière theory are obeyed.

We performed the following simulations: An electron was set in motion in a given direction, which defines the z-axis for the problem. A history was defined by having the total curved path, summed over all electron steps, exactly equal to the Molière upper limit. This was achieved by choosing the step to be a divisor of t_{max}. That is, one simulation was done with $t = t_{max}$, another with $t = t_{max}/2$, another with $t = t_{max}/3$, $\ldots t_{max}/N$, where N is an integer. The quantity "scored" was the average displacement along the z-axis, $\langle z \rangle_N$, at the end of the history. The sum of the curved paths of the N steps always equals t_{max}. We note that lateral displacements play no role in this simulation because they would average out to zero. We argue that *if the path-length correction and the Molière theory are both consistent, then the $\langle z \rangle_N$'s should be independent of N, or equivalently, step-size independent.*

We show two extreme cases in figs. 14.19 and 14.20. The former, for 10 MeV electrons in water, plots $\langle z \rangle_N$ versus the inverse number of steps, $1/N$. For contrast, the default path-length correction algorithm of EGS and simulations performed without a path-length correction are shown. Recall that there is no energy loss in these simulations. As an indicator of scale, we have included a line indicating the step-size (measured in $1/N$) equal to the CSDA range in water. We have seen before that at high energies,above 3 MeV in water, the Molière upper limit exceeds the CSDA range. We have also included the ESTEPE=20% line, approximately the default EGS step-size in water. If one used the default EGS simulation, one would make path-length related errors of only a few percent. The new path-length correction would allow the default upper limit on step-size in EGS to be extended upwards, allowing steps approaching the full CSDA range, without introducing artefacts! The new path-length correction thus shows a potential of speeding up high energy simulations! Benchmarks have yet to be performed in this area.

Figure 14.19: A test of the step-size dependence of the Molière theory with the new path-length correction and with other path-length correction methods. This case is for 10 MeV electrons in water.

Figure 14.20: A test of the step-size dependence of the Molière theory with the new path-length correction and with other path-length correction methods. This case is for 10 keV electrons in water.

Figure 14.20 depicts a similar set of simulations at 10 keV, three orders of magnitude less than the previous example. The ESTEPE=20% line, near the default EGS step-size, is close to the Molière upper limit. Path-length corrections are very important here. We also show Molière's lower limit, the $\Omega_0 = 20$ line. It was mentioned previously that Molière's lower limit was found to be too conservative and that sensible results could be expected for $\Omega_0 \geq e$. This is shown in fig. 14.20. The new path-length correction (or the Molière theory) show evidence of breakdown only in the vicinity of $\Omega_0 = e$. It is more likely, however, that this is a numerical problem as various functions, which become singular near this limit, are difficult to express numerically. Similar tests have been performed for other energies and materials. In all cases the step-size independence of the path-length correction and the Molière theory is demonstrated.

14.2.4 PRESTA's lateral correlation algorithm

In section 14.1.3, we discussed the importance of lateral transport for each electron step in certain calculations. Berger's algorithm [Ber63], eq. 17.4, is used by PRESTA. To test this algorithm, we used a test very similar to that used to prove the viability of the path-length correction of the previous section. Again, we modify our electron transport algorithm to conform with all the constraints of the Molière theory. Energy loss mechanisms were "switched off", all bounding surfaces were eliminated from the simulations to make it seem as if the transport took place in an infinite medium, and the step-size constraints of the Molière theory were obeyed. We performed the following simulations: An electron was set in motion in a given direction, which defines the z-axis for the problem. As before, a history was defined by having the total curved path, summed over all electron steps, exactly equal to the Molière upper limit. The quantity "scored" was the average displacement perpendicular to the z-axis, $\langle r \rangle_N$, at the end of the history. The sum of the curved paths of the N steps always equals t_{max}. Path-length corrections play a minor role in these simulations because the geometric straight-line transport distances are somewhat dependent upon the amount of curvature correction applied to the electron steps. However, as shown in the previous section, the path-length correction and the Molière theory are both consistent. If the lateral correlation algorithm is also consistent, then the $\langle r \rangle_N$'s should also be independent of N, or equivalently, step-size independent.

We show one representative case in fig. 14.21 for 100 keV electrons in water, which depicts $\langle r \rangle_N$ versus the inverse number of steps, $1/N$. We also show two other calculations of r_N which do not include the lateral correlation algorithm. One is the default EGS calculation with its default path-length correction and the other has no path-length correction. The relatively small difference between these two curves indicates that this test depends only weakly upon the path-length correction used. (If the new path-length correction was used without a lateral correlation algorithm, it would lie somewhere between these two curves.) A great reduction of step-size dependence in this calculation is demonstrated. Only for

Figure 14.21: Step-size independence test of the lateral correlation algorithm. Also shown are two calculations without lateral displacements, with and without the default EGS path-length correction. This test depends only weakly upon the path-length correction used. This case is for 100 keV electrons in water.

the large step-sizes is there any evidence of deviation. This feature has been observed at all energies [BR87]. However, we shall see in the next section that the remaining dependence is eliminated when energy loss is incorporated. The "ESTEPE=20%" line shows the approximate step-size used by EGS in its default configuration.

14.2.5 Accounting for energy loss

The underlying Molière theory does not treat energy loss directly. Actually, it is not too difficult to use the Molière theory in a more general fashion and incorporate energy loss. One merely has to convert integral equations in the following fashion:

$$\int_0^t dt' f(t', E(t')) \Longrightarrow \int_{E_f}^{E_0} dE' f\left(t'(E'), E'\right) / |s(E')|, \tag{14.4}$$

where $f()$ is any function of the curved path-length, t, and the energy, E. The function, s(), is the stopping power. The familiar equation relating E and t directly is obtained by making the substitution, $f() \rightarrow 1$ in the above equation. However, such equations prove to be difficult to handle numerically and it is not really necessary. In all the formulae used in regards to multiple scattering and the various elements of PRESTA, an integration over t' is involved. It is then sufficiently accurate to make the approximation that the energy is constant if it is evaluated at the midpoint of the step. In more concrete terms, we approximate,

$$\int_0^t dt' f\left(t', E(t')\right) \approx \int_0^t dt' f(t', \tilde{E}), \tag{14.5}$$

where $\tilde{E} = \frac{1}{2}[E_0 + ts(\tilde{E})]$. Note that this latter equation for $\tilde{E}$ is really an iterative equation and it has been found that it is sufficient to evaluate it only to first order. That is, we make the approximation that $\tilde{E} \approx \frac{1}{2}\{E_0 + ts(\frac{1}{2}[E_0 + ts(E_0)])\}$. Some justification for this treatment can be obtained from the following relation,

$$I = \int_{E_f}^{E_0} dE\ f(E) = \Delta E \left\{ f(\tilde{E}) + \frac{1}{24}(\Delta E)^2 f''(\tilde{E}) \ldots \right\}, \tag{14.6}$$

where $\tilde{E} = (E_0 + E_f)/2$, $\Delta E = E_0 - E_f$, and $f''(E)$ is the second derivative of with respect to E. Thus, if ΔE is not large with respect to E, and $f''()$ is not too large, the approximation, $I \approx \Delta E f(\tilde{E})$ is valid.

Further justification may be obtained by viewing the step-size independence of $\langle z \rangle_N$ and $\langle r \rangle_N$ with energy loss incorporated by the above method *i.e.* evaluating all energy-related expressions at the mid-point of the step. The results are shown in figs. 14.22 and 14.23, respectively. In each case, the step-size was chosen to be a fixed value of Molière's upper limit. However, as the particle loses energy this step-size changes owing to it's inherent energy dependence. In each case, the electron's endpoint energy, at which point the transport was

Figure 14.22: A similar test of the path-length correction done for figs. 14.19 and 14.20 but with energy loss incorporated. Electron histories were terminated when the kinetic energy, EKCUT, reached 1% of the starting energy, except in the 10 keV case where it was 10%.

Figure 14.23: A similar test of the lateral correlation done for fig. 14.21 but with energy loss incorporated. Electron histories were terminated when the kinetic energy, EKCUT, reached 1% of the starting energy, except in the 10 keV case where it was 10%.

terminated, was chosen to be 1% of the starting energy. The only exception was 10 keV, where the endpoint energy was 1 keV. We note that both $\langle z \rangle_N$ and $\langle r \rangle_N$ exhibit step-size independence. Even more remarkable is the fact that the minor step-size dependence exhibited by $\langle r \rangle_N$, shown in fig. 14.21, has vanished. This improvement appears to be fortuitous resulting form cancellations of second-order effects. More research is needed to study the theories concerning lateral displacements.

14.2.6 PRESTA's boundary crossing algorithm

The final element of PRESTA is the boundary crossing algorithm. This part of the algorithm tries to resolve two irreconcilable facts: that electron transport must take place across boundaries of arbitrary shape and orientation, and that the Molière multiple scattering theory is invalid in this context.

If computing speed did not matter, the solution would be obvious—use as small a step-size as possible within the constraints of the theory. With this method, a great majority of the transport steps would take place far removed from boundaries and the underlying theory would only be "abused" for that small minority of steps when the transport takes place in the direct vicinity of boundaries. This would also solve any problems associated with the omission of lateral translation and path-length correction. However, with the inclusion of a reliable path-length correction and lateral correlation algorithm, we have seen that we may simulate electron transport with very large steps in infinite media. For computing efficiency, we wish to use these large steps as often as possible.

Consider what happens as a particle approaches a boundary in the PRESTA algorithm. First we interrogate the geometry routines of the transport code and find out the closest distance to any boundary. As well as any other restrictions on electron step-size, we restrict the electron step-size, (total, including path-length curvature) to the closest distance to any boundary. We choose to restrict the *total* step-size so that no part of the electron path could occur across any boundaries. We then transport the particle, apply path-length corrections, the lateral correlation algorithm, and perform any "scoring" we wish to do. We then repeat the process.

At some point this process must stop, else we encounter a form of Zeno's paradox. We will never reach the boundary! We choose a minimum step-size which stops this sort of step-size truncation. We call this minimum step-size t'_{min}. If a particle's step-size is restricted to t'_{min}, we are in the vicinity of a boundary. The particle may or *may not* cross it. At this point, to avoid ambiguities, the lateral correlation algorithm is switched off, whether or not the particle actually crosses the boundary. If we eventually cross the boundary, we transport the particle with the same sort of algorithm. We *start* with a step t'_{min}. We then let the above algorithm take over. This process is illustrated in fig. 14.24. This example is for a 10 MeV electron incident normally upon a 1 cm slab of water. The first step is t'_{min} in length.

Figure 14.24: Boundary crossing algorithm example: A 10 MeV electron enters a 1 cm slab of water from the left in the normal direction. The first step is t'_{min} in length. Since the position here is less than t'_{min} away from the boundary, the next step is length t'_{min} as well. The next 4 steps are approximately $2t'_{min}$, $4t'_{min}$, $8t'_{min}$, and $16t'_{min}$ in length, respectively. Finally, the transport begins to be influenced by the other boundary, and the steps are shortened accordingly. The electron leaves the slab in 3 more steps.

Since the position at this point is less than t'_{min} away from the boundary (owing to path curvature), the next step is length t'_{min} as well. The next 4 steps are approximately $2t'_{min}$, $4t'_{min}$, $8t'_{min}$, and $16t'_{min}$ in length, respectively. Finally, the electron begins to "see" the other boundary, shortens its steps accordingly. For example, the total curved path "a" in the figure is associated with the transport step "b". The distance "a" is the distance to the closest boundary.

Finally, what choice should be made for t'_{min}? One could choose t'_{min}= t_{min}, the minimum step-size constraint of the Molière theory. Although this option is available to the PRESTA user, practice has shown it to be too conservative. Larger transport steps may be used in the vicinity of boundaries. The following choice, the default setting for t'_{min}, has been found to be be a good practical choice, allowing both accurate calculation and computing efficiency: Choose t'_{min} to equal t_{max} for the minimum energy electron in the problem (as set by transport cut-off limits). Then scale the energy-dependent parts of the equation for t'_{min} accordingly, for higher energy electrons. The reader is referred to ref. [BR87] for the mathematical details. As an example, we return to the "air tube" calculation of fig. 14.16. In that figure, the choice of "blcmin", the variable in PRESTA which controls the boundary crossing algorithm and which is closely related to t'_{min}, was set to 1.989. This causes t'_{min} to be equal to t_{max} for 2 keV electrons. A transport cut-off of 2 keV is appropriate in this simulation because electrons with this energy have a range which is a fraction of the diameter of the tube. In most practical problems, if one chooses the transport cut-off realistically, PRESTA's default selection for t'_{min} produces accurate results. Again, the reader is referred to the PRESTA documentation [BR87] for further discussion.

PRESTA, as the name implies, was designed to calculate quickly as well as accurately, since it wastes little time taking small transport steps in regions where it has no need to. There is no space to go into further discussion about this although there is a brief discussion in Chapter 17. Again, the reader is referred elsewhere [BR87]. Typical timing studies have shown that PRESTA, in its standard configuration, executes as quickly, and sometimes much more quickly, then EGS with ESTEPE set so as to produce accurate results. For problems with a fine mesh of boundaries, for example a depth-dose curve with a $r_0/40$ mesh, the timing is about the same. For other problems, with few boundaries, the gain in speed is about a factor of 5.

14.2.7 Caveat Emptor

It would leave the reader with a mistaken impression if the chapter was terminated at this point. PRESTA has demonstrated that step-size dependence of calculated results has been eliminated in many cases and that computing time can be economized as well. By understanding the elements of condensed-history electron transport, some problems have been solved. Calculational techniques that isolate the effects of various constituents of the electron transport algorithm have been developed and used to prove their step-size independence. However, PRESTA is not the final answer because it does not solve all step-size dependence problems, in particular, backscattering. This is demonstrated by the example shown in fig. 14.25. In this example, 1.0 MeV electrons were incident normally on a semi-infinite slab of water. The electron transport was performed in the CSDA approximation. That is, no δ-rays or bremsstrahlung γ's were set in motion and the unrestricted collision stopping power was used. The ratio of backscattered kinetic energy to incident kinetic energy was calculated. The default EGS calculation (with ESTEPE control) is shown to have a large step-size dependence. The PRESTA calculation is much improved but still exhibits some residual dependence on step-size.

In general, problems that depend strongly on backscatter will exhibit a step-size dependence, although the severity is much reduced when one uses PRESTA. We may speculate on the reason for the existence of the remaining step-size dependence. Recall that the path-length correction, which relates the straight-line path length, s, and t, the curved path-length of the transport step, really calculates only an average value. That is, given t, the value of s is predetermined and unique. It is really a distributed quantity and should be correlated to the multiple scattering angle of the step. In other words, we expect the distribution to be peaked in the backward direction if $\Theta = \pi$ and peaked in the forward direction if $\Theta = 0$. To this date, distributions of this sort which are accurate for large angle scattering are unknown. If they are discovered they may cure PRESTA's remaining step-size dependence.

Figure 14.25: Fractional energy backscattered from a semi-infinite slab of water with 1.0 MeV electrons incident normally. The electron transport was performed in the CSDA approximation. (No δ-rays or γ's were set in motion). The default EGS and PRESTA calculations are contrasted. There is still evidence of step-size dependence in the PRESTA calculation.

Bibliography

[Ber63] M. J. Berger. Monte Carlo Calculation of the penetration and diffusion of fast charged particles. *Methods in Comput. Phys.*, 1:135 – 215, 1963.

[Bet53] H. A. Bethe. Molière's theory of multiple scattering. *Phys. Rev.*, 89:1256 – 1266, 1953.

[BR87] A. F. Bielajew and D. W. O. Rogers. PRESTA: The Parameter Reduced Electron-Step Transport Algorithm for electron Monte Carlo transport. *Nuclear Instruments and Methods*, B18:165 – 181, 1987.

[BRN85] A. F. Bielajew, D. W. O. Rogers, and A. E. Nahum. Monte Carlo simulation of ion chamber response to ^{60}Co – Resolution of anomalies associated with interfaces,. *Phys. Med. Biol.*, 30:419 – 428, 1985.

[BS83] M. J. Berger and S. M. Seltzer. Stopping power and ranges of electrons and positrons. *NBS Report NBSIR 82-2550-A (second edition)*, 1983.

[Eyg48] L. Eyges. Multiple scattering with energy loss. *Phys. Rev.*, 74:1534, 1948.

[Fan54] U. Fano. Note on the Bragg-Gray cavity principle for measuring energy dissipation. *Radiat. Res.*, 1:237 – 240, 1954.

[GS40a] S. A. Goudsmit and J. L. Saunderson. Multiple scattering of electrons. *Phys. Rev.*, 57:24 – 29, 1940.

[GS40b] S. A. Goudsmit and J. L. Saunderson. Multiple scattering of electrons. II. *Phys. Rev.*, 58:36 – 42, 1940.

[HW55] D. F. Hebbard and R. P. Wilson. The effect of multiple scattering on electron energy loss distribution. *Aust. J. Phys.*, 8:90 –, 1955.

[Lew50] H. W. Lewis. Multiple scattering in an infinite medium. *Phys. Rev.*, 78:526 – 529, 1950.

[Mol47] G. Z. Molière. Theorie der Streuung schneller geladener Teilchen. I. Einzelstreuung am abgeschirmten Coulomb-Field. *Z. Naturforsch*, 2a:133 – 145, 1947.

[Mol48] G. Z. Molière. Theorie der Streuung schneller geladener Teilchen. II. Mehrfach- und Vielfachstreuung. *Z. Naturforsch*, 3a:78 – 97, 1948.

[NHR85] W. R. Nelson, H. Hirayama, and D. W. O. Rogers. The EGS4 Code System. Report SLAC–265, Stanford Linear Accelerator Center, Stanford, Calif, 1985.

[RBN85] D. W. O. Rogers, A. F. Bielajew, and A. E. Nahum. Ion chamber response and A_{wall} correction factors in a ^{60}Co beam by Monte Carlo simulation. *Phys. Med. Biol.*, 30:429 – 443, 1985.

[Rog84] D. W. O. Rogers. Low energy electron transport with EGS. *Nucl. Inst. Meth.*, 227:535 – 548, 1984.

[SA55] L. V. Spencer and F. H. Attix. A theory of cavity ionization. *Radiat. Res.*, 3:239 – 254, 1955.

[Yan51] C. N. Yang. Actual path length of electrons in foils. *Phys. Rev*, 84:599 – 600, 1951.

Problems

1.

Chapter 15

Advanced electron transport algorithms

In this chapter we consider the transport of electrons in a condensed history Class II scheme [Ber63]. That is to say, the bremsstrahlung processes that result in the creation of photons above an energy threshold E_γ, and Møller knock-on electrons set in motion above an energy threshold E_δ, are treated discretely by creation and transport. Sub-threshold processes are accounted for in a continuous slowing down approximation (CSDA) model. For further description of the Class II scheme the reader is encouraged to read Berger's article [Ber63] who coined the terminology and gave a full description and motivation for the classification scheme. Figure 15.1 gives a graphical description of the transport.

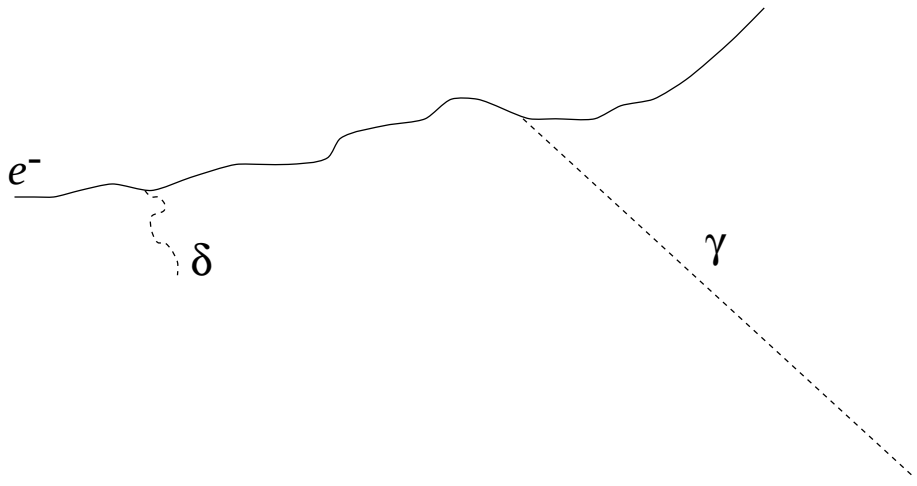

Figure 15.1: This is a depiction of a complete electron history showing elastic scattering, creation of bremsstrahlung above the E_γ threshold, the setting in motion of a knock-on electron above the E_δ threshold and absorption of the primary and knock-on electrons.

The electron transport processes between the particle creation, absorption vertices is governed by the Boltzmann transport equation as formulated by Larsen [Lar92]:

$$\left[\frac{1}{v}\frac{\partial}{\partial t} + \vec{\Omega}\cdot\vec{\nabla} + \sigma_{\rm s}(E) - \frac{\partial}{\partial E}L(E)\right]\psi(\vec{x},\vec{\Omega},E,t) = \int_{4\pi}\mathrm{d}\Omega'\,\sigma_{\rm s}(\vec{\Omega}\cdot\vec{\Omega}',E)\psi(\vec{x},\vec{\Omega}',E,t)\ , \quad (15.1)$$

where $\vec{x}$ is the position, $\vec{\Omega}$ is a unit vector indicating the direction of the electron, E is the energy of the electron and t is time. $\sigma_{\rm s}(\vec{\Omega}\cdot\vec{\Omega}',E)$ is the macroscopic differential scattering cross section,

$$\sigma_{\rm s}(E) = \int_{4\pi}\mathrm{d}\Omega'\,\sigma_{\rm s}(\vec{\Omega}\cdot\vec{\Omega}',E) \quad (15.2)$$

is the total macroscopic cross section (probability per unit length), $L(E)$ is the restricted stopping power appropriate for bremsstrahlung photon creation and Møller electrons beneath their respective thresholds E_γ and E_δ, v is the electron speed and $\psi(\vec{x},\vec{\Omega},E,t)\,\mathrm{d}\vec{x}\,\mathrm{d}\Omega\,\mathrm{d}E$ is the probability of there being an electron in $\mathrm{d}\vec{x}$ about $\vec{x}$, in $\mathrm{d}\Omega$ about $\vec{\Omega}$ and in $\mathrm{d}E$ about E at time t. The boundary condition to be applied to each segment in Figure 15.1 is:

$$\psi(\vec{x},\vec{\Omega},E,0) = \delta(\vec{x})\delta(\hat{z}-\vec{\Omega})\delta(E_n - E)\ , \quad (15.3)$$

where the start of each segment is translated to the origin and rotated to point in the z-direction. ($\hat{z}$ is a unit vector pointing along the z-axis.) The energy at the start of the n-th segment is E_n.

For our considerations within the CSDA model, we note that E and t can be related since the pathlength, s,

$$s = vt = \int_E^{E_n}\frac{\mathrm{d}E'}{L(E')}, \quad (15.4)$$

permitting a slight simplification of Eq. 15.1:

$$\left[\frac{\partial}{\partial s} + \vec{\Omega}\cdot\vec{\nabla} + \sigma_{\rm s}(E)\right]\psi(\vec{x},\vec{\Omega},s) = \int_{4\pi}\mathrm{d}\Omega'\,\sigma_{\rm s}(\vec{\Omega}\cdot\vec{\Omega}',E)\psi(\vec{x},\vec{\Omega}',s)\ . \quad (15.5)$$

The cross section still depends on E which may be calculated from Eq. 15.4.

Lewis [Lew50] has presented a "formal" solution to Eq.15.5. By assuming that ψ can be written in an expansion in spherical harmonics,

$$\psi(\vec{x},\vec{\Omega},s) = \sum_{lm}\psi_{lm}(\vec{x},s)Y_{lm}(\vec{\Omega})\ , \quad (15.6)$$

one finds that

$$\left[\frac{\partial}{\partial s} + \kappa_l\right]\psi_{lm}(\vec{x},s) = -\sum_{\lambda\mu}\vec{\nabla}\psi_{\lambda\mu}(\vec{x},s)\cdot\vec{Q}_{lm}^{\lambda\mu}\ , \quad (15.7)$$

where

$$\kappa_l(E) = \int_{4\pi}\mathrm{d}\Omega'\,\sigma_{\rm s}(\vec{\Omega}\cdot\vec{\Omega}',E)[1 - P_l(\vec{\Omega}\cdot\vec{\Omega}')]\ , \quad (15.8)$$

and

$$\vec{Q}_{lm}^{\lambda\mu} = \int_{4\pi} \mathrm{d}\Omega \, Y_{lm}^{*}(\vec{\Omega}) \, \vec{\Omega} \, Y_{\lambda\mu}(\vec{\Omega}) \ . \tag{15.9}$$

If one considers angular distribution only, then one may integrate over all $\vec{x}$ in Eq. 15.7 giving:

$$\left[\frac{\partial}{\partial s} + \kappa_l \right] \psi_l(s) = 0 \ , \tag{15.10}$$

resulting in the solution derived by Goudsmit and Saunderson [GS40a, GS40b]:

$$\psi(\vec{\Omega}, s) = \frac{1}{4\pi} \sum_l (2l+1) P_l(\hat{z} \cdot \vec{\Omega}) \exp\left(- \int_0^s \mathrm{d}s' \, \kappa_l(E) \right) \ . \tag{15.11}$$

Eq. 15.7 represents a complete formal solution of the Class II CSDA electron transport problem but it has never been solved exactly. However, Eq. 15.7 may be employed to extract important information regarding the moments of the distributions. Employing the definition,

$$k_l(s) = \exp\left(- \int_0^s \mathrm{d}s' \, \kappa_l(E) \right) \ , \tag{15.12}$$

Lewis [Lew50] has shown the moments $\langle z \rangle$, $\langle z \cos\Theta \rangle$, and $\langle x^2 + y^2 \rangle$ to be:

$$\langle z \rangle = \int_0^s \mathrm{d}s' \, k_1(s') \ , \tag{15.13}$$

$$\langle z \cos\Theta \rangle = \frac{k_1(s)}{3} \int_0^s \mathrm{d}s' \, \frac{1 + 2k_2(s')}{k_1(s')} \ , \tag{15.14}$$

and

$$\langle x^2 + y^2 \rangle = \frac{4}{3} \int_0^s \mathrm{d}s' \, k_1(s') \int_0^{s'} \mathrm{d}s'' \, \frac{1 - k_2(s'')}{k_1(s'')} \ . \tag{15.15}$$

It can also be shown using Lewis's methods that

$$\langle z^2 \rangle = \frac{2}{3} \int_0^s \mathrm{d}s' \, k_1(s') \int_0^{s'} \mathrm{d}s'' \, \frac{1 + 2k_2(s'')}{k_1(s'')} \ , \tag{15.16}$$

and

$$\langle x^2 + y^2 + z^2 \rangle = 2 \int_0^s \mathrm{d}s' \, k_1(s') \int_0^{s'} \mathrm{d}s'' \, \frac{1}{k_1(s'')} \ , \tag{15.17}$$

which gives the radial coordinate after the total transport distance, s. Note that there was an error[1] in Lewis's paper where the factor 1/3 was missing from his version of $\langle z \cos\Theta \rangle$. In the

[1]The correction of Lewis's Eq. 26 is:

$$H_{l1} = \sqrt{\frac{1}{4\pi(2l+1)}} k_l(s) \int_0^s \mathrm{d}s' \, \frac{l k_{l-1}(s') + (l+1) k_{l+1}(s')}{k_1(s')}$$

The reader should consult Lewis's paper [Lew50] for the definition of the H-functions.

limit that $s \longrightarrow 0$, one recovers from Eqs. 15.14 and 15.16 the results $\lim_{s \longrightarrow 0}\langle z \cos\Theta\rangle = s$ and $\lim_{s \longrightarrow 0}\langle z^2\rangle = s^2$ which are not obtained without correcting the error as described in the footnote. Similar results for the moments have been derived recently by Kawrakow [Kaw96a] using a statistical approach.

Before leaving this introductory section it warrants repeating that these equations are all "exact" within the CSDA model and are independent of the form of the elastic scattering cross section. It should also be emphasized that Larsen analysis [Lar92] proves that the condensed history always gets the correct answer (consistent with the validity of the elastic scattering cross section) in the limit of small step-size providing that the "exact" Goudsmit-Saunderson multiple-scattering formalism is employed (and that its numerical stability problems at small step-size can be solved). Larsen analysis also draws some conclusions about the underlying Monte Carlo transport mechanisms and how they relate to convergence of results to the correct answer. Some Monte Carlo techniques can be expected to be less step-size dependent than others and converge to the correct answer more efficiently, using larger steps.

The ultimate goal of a Monte Carlo transport algorithm should be to make electron condensed history calculations as stable as possible with respect to step-size. That is, for a broad range of applications there should be step-size *independence* of the result. Hence, it would be most efficient to use steps as large as possible and not be subject to calculation errors. While we have not yet achieved this goal, we have made much progress towards it and describe some of this progress in a later section.

15.1 What does condensed history Monte Carlo do?

Monte Carlo calculations attempt to solve Eq. 15.5 iteratively by breaking up the transport between discrete interaction vertices, as depicted in Figure 15.2. The first factor determining the electron step-size distance is the distance to a discrete interaction. These distances are stochastic and characterized by an exponential distribution. Further subdivision schemes may be employed and these can be classified as numeric, physics' or boundary step-size constraints.

15.1.1 Numerics' step-size constraints

A geometric restriction, say $s \leq s_{\max}$ may be used.A geometric restriction of this form was introduced by Rogers [Rog84b] in the EGS Monte Carlo code [NHR85, BHNR94]. This has application in graphical displays of Monte Carlo histories. One wants the electron tracks to have smooth lines and so the individual pathlengths should be of the order of the resolution size of the graphics display. Otherwise, the tracks look artificially jagged, as they do in Figure 15.2. Of course, there are some real sharp bends in the electron tracks associated with large angle elastic scattering, but these are usually infrequent. One can predict the

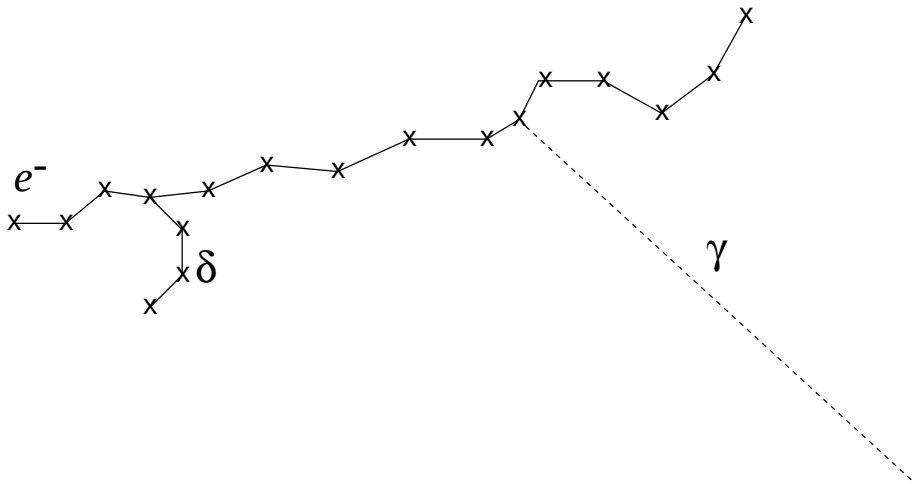

Figure 15.2: This is how a Monte Carlo calculates of the complete electron history as depicted in Figure 15.1. The transport takes place in steps, the vertices of which are marked with the symbol "×".

number of steps required to follow a particle to termination. For this case $N = r(E_{\rm i})/s_{\rm max}$, where $r(E_{\rm i})$ is the range of an electron with starting energy $E_{\rm i}$.

Another popular choice is a constant fractional energy loss per electron step, *i.e.* $\Delta E/E =$ constant. This has a slight disadvantage that the electron steps get shorter and shorter as the energy of the electrons in the simulation gets smaller and smaller. In terms of the dynamic range of the energies of the particles in the simulation, generally the lower ones play a lesser important role (there are exceptions to this of course!) and so, despite its popularity, it is probably wasteful in many applications. One can predict the number of steps required to follow a particle to termination in this case as well. For this case $N = log(1 - \Delta E/E)/log(E{\rm min}/E_{\rm i})$ where Emin is the minimum electron energy for which transport takes place. One sees that as Emin is pushed downwards by the requirements of some applications, that the number of steps acquires a slow logarithmic growth, unlike the geometric restriction. The constant fractional energy loss per electron step is built into the ETRAN Monte Carlo code [Ber63, Sel89, Sel91] and its well-known progeny, the ITS system [HKM$^+$92] and the electron component of MCNP [Bri86, Bri93]. In these code systems, the value of the constant is kept in internal tables and its value determined through trial and error. In the EGS system [NHR85, BHNR94], it is available to the user as a "tuning" parameter, to be adjusted (lowered) until the answer converges to the (presumably correct) result.

There are other schemes of step-size restriction that will not be discussed. However, we see that the two discussed thus far play the role of an "integration mesh-density". To get better results one must increase the resolution. To be practical, the mesh density ought to be as large as possible, consistent with target accuracy of the application. Larsen [Lar92] has made an interesting analysis of Monte Carlo algorithms and how they should be expected

to converge. He showed that the ETRAN scheme proposed by Berger [Ber63] contains $O(\Delta s)$ errors. Thus, one expects that accurate calculation with ETRAN methods would converge slowly and require small step-sizes to get the answer correct. Indeed, this was the case with the EGS code as well, motivating the step-size restrictions introduced into EGS by Rogers [Rog84b].

Larsen [Lar92] also proposed an alternative Monte Carlo method (calling it "Method 3") to enable faster convergence since it contains $O(\Delta s^2)$ errors. The algorithm for each sub-step, Δs, is that first it must be broken into two parts. The first part is a drift of length $\Delta s/2$ in the initial direction of motion, and a deduction in energy due to continuous energy losses over the first part of this step. The multiple-scattering angle is sampled at this new energy but for a deflection angle assuming that the particle as gone the full sub-step distance, Δs, and deflection by this angle. The sub-step is then completed by executing a drift of distance $\Delta s/2$ in the new direction. Although this method may seem as is if is doubling the number of steps, this is actually not the case since the most computer-intensive part of the process, namely sampling the multiple-scattering angle and rotation, is performed only once per sub-step.

The result of the "Method 3" procedure is to impart longitudinal and lateral distributions to the sub-step, both correlated to the multiple-scattering angle, Θ. Assuming the particle starts at the origin and is directed along the z-axis, after a total sub-step pathlength of Δs, the final resting place will be:

$$\begin{aligned} \Delta x &= (\Delta s/2)\sin\Theta\cos\Phi \\ \Delta y &= (\Delta s/2)\sin\Theta\sin\Phi \\ \Delta z &= (\Delta s/2)(1+\cos\Theta)\ , \end{aligned} \tag{15.18}$$

where Φ is a randomly selected azimuthal angle and it is understood that Θ is sampled from the Goudsmit-Saunderson [GS40a, GS40b] multiple-scattering theory at the mid-point energy.

Only two previously published Monte Carlo methods have followed this prescription. Berger's method [Ber63] is similar except that he proposed a straggling term for the lateral components and the energy dependence was taken account for directly. However, the longitudinal and lateral distributions have only been recently been implemented into ETRAN [Sel91].

The other method is the PRESTA algorithm [BR86, BR87] that has been incorporated into EGS. This algorithm is different from Method-3 in that the final longitudinal position was determined by its average rather than the distribution implied by Eq. 15.18. However, this only contributes to the $O(\Delta s^2)$ error. The other very important distinction is that the PRESTA algorithm employs the Molière multiple-scattering method method [Mol47, Mol48] with corrections and limitations discussed by Bethe [Bet53].

There has also been a recently-published method called the Longitudinal and Lateral Correlation Algorithm (LLCA) proposed by Kawrakow [Kaw96a]. It incorporates the Method-3

transport scheme except that the multiple-scattering theory, while representing an improvement over Molière's method is still an approximation [Kaw96b] to the Goudsmit-Saunderson method. However, there is one important improvement over Method-3 in that the lateral position of the electron at the end of the sub-step is connected to the multiple-scattering angle by means of a distribution, rather than direct correlation as implied by Eq. 15.18. For the present, this distribution function has only been calculated using single-scattering methods (analog Monte Carlo or event-by-event elastic scattering). Presumably, this is an $O(\Delta s^2)$ or higher correction.

15.1.2 Physics' step-size constraints

There are also step-size restrictions related to keeping the step-sizes within range of the validity of the theories underlying the condensed history method. This is important, for example, when using the Molière multiple-scattering theory [Mol47, Mol48]. Bethe [Bet53] analyzed Molière multiple-scattering theory, comparing it to the "exact" theory of Goudsmit and Saunderson [GS40a, GS40b] and provided a correction that improves the large-angle behaviour of Molière theory for large angles as Molière theory is couched in the small-angle formalism of Bothe [Bot21] and Wentzel [Wen22]. The electron step-size constraint arises from not allowing the multiple-scattering angle to attain values greater than 1 radian.

Small-angle multiple scattering theories still play an important role in electron Monte Carlo calculations of the Class II variety since Class II condensed history techniques sample the multiple-scattering distributions "on-the-fly" as the pathlength can, in principle be anything within the constraints already discussed. Class I algorithms, as defined in Berger's work [Ber63], demand that the electrons follow a predetermined energy grid, allowing the multiple-scattering distributions to be pre-calculated. While Class I and Class II have their attributes and shortcomings, the use of an approximate multiple-scattering theory in Class II calculations, considered with the conclusion of the previous section, forces the realization that one can not necessarily expect that the limit of small step-size will produce the correct answer for Class-II/approximate multiple-scattering algorithms! It should also be remarked that Class-I/exact multiple-scattering schemes are subject to numerical instabilities as smaller step-sizes require an increasing number of terms in the Legendre serious of Eq. 15.11 to be summed. There have been studies demonstrating that one can converge to the incorrect answer in a Class-II/approximate multiple-scattering algorithm [Rog93, Bie96].

Step-size instability of the Molière theory [Mol48] has been studied extensively [AMB93, Bie94] and comparisons with Goudsmit-Saunderson theory [GS40a, GS40b] have been performed [Bet53, Win87] as well as comparisons with single-elastic scattering Monte Carlo [Bie94]. This has motivated the development of a new multiple-scattering theory based on Goudsmit-Saunderson theory [GS40a, GS40b] but formulated in such a way as to allow sampling "on-the-fly" as required by Class II algorithms and eliminating the small step-size numerical instability of the Goudsmit-Saunderson Legendre summation that arises

from the form expressed in Eq. 15.11. This recent work [KB98] will be discussed in a later section. However, this new multiple-scattering theory will guarantee that condensed history Monte Carlo will always converge to the correct answer in the limit of small electron step-size.

15.1.3 Boundary step-size constraints

The final category of electron step-size constraint we consider relates to the geometry, specifically interfaces and material boundaries. Although the transport theory expressed in Eq. 15.5 and the various solutions to it describe electron transport in infinite, unbounded uniform media, practical applications contain boundaries and interfaces between media. Except for the stopping of electrons at interfaces and the updating the material-dependent transport data, this problem was not considered until the EGS/PRESTA algorithm was developed [BR86, BR87]. This algorithm requires knowledge of the nearest distance to any interface and shortens the electron step-size accordingly, by setting $s = s^{\perp}_{\min}$ where $s^{\perp}_{\min}$ is the nearest distance to any interface. This is always a perpendicular distance (as suggested by the notation) unless the closest distance happens to be along an intersection of two surfaces. This procedure requires more information from the geometry[2] but it is necessary to avoid potential misuse of the underlying transport theory. Of course this shortening can not continue indefinitely as the electron would never reach the surface, a transport equivalent of Xeno's paradox. PRESTA continues the procedure until the transport steps approach the lower limit of validity of Molière theory, usually from about 3 to 20 mean-free-path distances, and then allows the electron to reach the surface, does not model the lateral components of sub-step transport given in Eq. 15.18 (This is a necessary part of the transport logic, otherwise the lateral transport takes the electron away from the surface, in either medium), updates material-dependent data and carries on in the next medium. The initial distance is again related to the lower limit of validity of Molière theory and thereafter the algorithm adjusts step-sizes according to $s^{\perp}_{\min}$. As a particle recedes from a boundary, its steps grow and grow, allowing for efficient, rapid transport away from interfaced. This behaviour is depicted in Figure 15.3.

However, this technique is not without its difficulties. Because lateral transport is not modeled for the steps that touch the boundary, the multiple-scattering deflection is performed at the end of the sub-step. Electron can thus backscatter from a surface, requiring careful handling of the transport logic in the vicinity of interfaces [Bie95]. This "boundary-crossing algorithm" as implemented in PRESTA also pushes the Molière theory towards the edge of its region of validity. Granted, the misuse of Molière theory is minimized but it still exists.

[2]The general requirements for electron transport in a geometry composed entirely of planar and quadric surfaces (*i.e.* spheroids, cones, hyperboloids, paraboloids) has recently been developed [Bie95]. Although the distance of intersection to any quadric surface along the particle trajectory requires finding the root of a quadratic equation, the nearest distance to a quadric surface is the root of an n^{th}-order equation where $n \leq 6$!

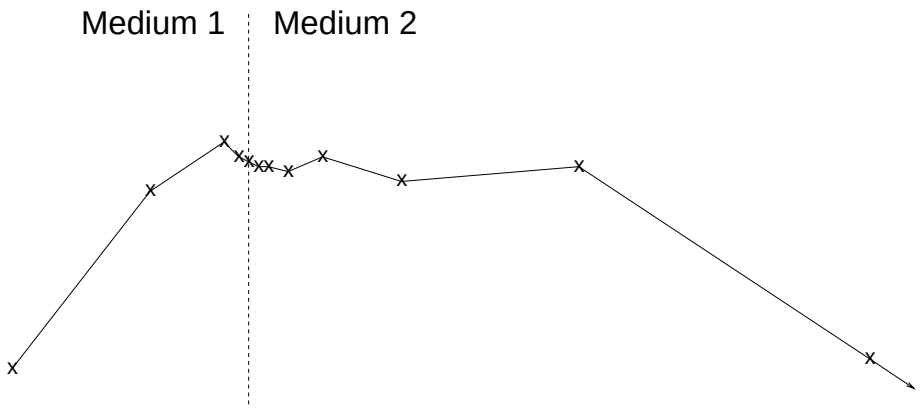

Figure 15.3: This is a depiction of operation of the PRESTA algorithm, which adjusts electron step-sizes in the vicinity of boundaries.

A more fundamental shortcoming was pointed out by Foote and Smyth [FS95] who pointed out that the deflection at the interface can cause a spurious events whereby an electron, having crossed a boundary can assume a trajectory that is parallel, or nearly so, to the surface at this point. The artefact shows up interfaces between condensed materials and gases. An electron penetrating the gas may be scattered into a near-parallel trajectory with the boundary. Even step-sizes of the order of several mean-free-path distances may be too large in the gas.

This artefact can be eliminated through use of a condensed history method that "evaporates" to a single-scattering method in the vicinity of interfaces [Bie96]. The algorithm is sketched in Figure 15.4. Using the new method, the only way that an electron can cross the interface is through a "no scatter drift" across the interface which involves no approximation. This technique, coupled with the new multiple-scattering theory will allow for error-free Monte Carlo calculations in the limit of small step-size in applications with arbitrarily complex geometries, interfaces and media.

15.2 The new multiple-scattering theory

The "exact" multiple-scattering angular distribution of Eq. 15.11 may be integrated easily over azimuthal angles (assuming that the cross section does not depend on polarisation) and written:

$$\psi(\cos\Theta, s) = \sum_l (l + 1/2) P_l(\cos\Theta) \exp\left(-\int_0^s \mathrm{d}s'\, \kappa_l(E)\right) \ , \tag{15.19}$$

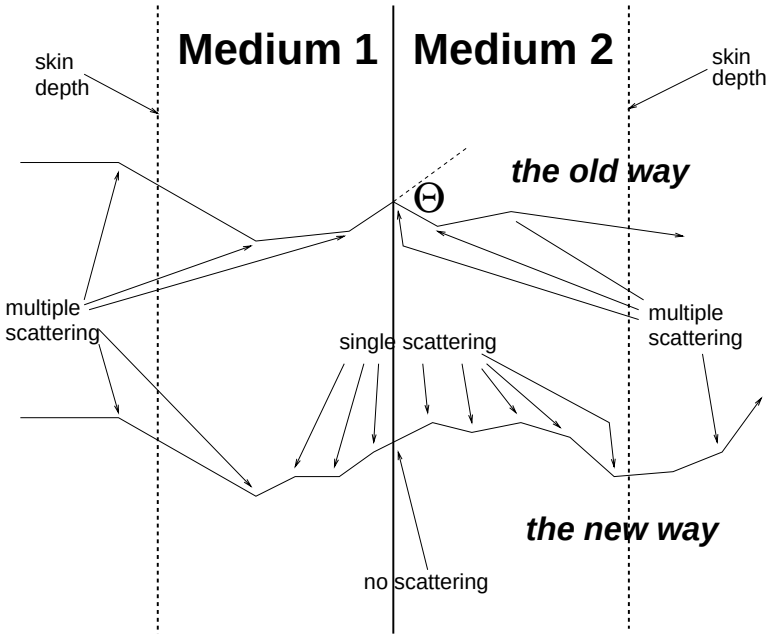

Figure 15.4: This is a depiction of the new boundary-cross algorithm which eliminates boundary-related artefacts.

and then reorganized in the following form [KB98]:

$$\psi(\cos\Theta, s) = e^{-\lambda}\delta(1-\cos\Theta)+\lambda e^{-\lambda}\tilde{\sigma}+(1-e^{-\lambda}-\lambda e^{-\lambda})\sum_l (l+1/2)P_l(\cos\Theta)\frac{e^{-\lambda g_l}-1-\lambda g_l}{e^{-\lambda}-1-\lambda}\ , \tag{15.20}$$

where

$$\lambda = \int_0^s \mathrm{d}s'\,\sigma_\mathrm{s}(E) \tag{15.21}$$

is the distance measured in mean-free-path taking into account the change in energy of the scattering cross section, and $e^{-\lambda}$ is the probability that the electron can go a distance λ without scattering even once,

$$\tilde{\sigma} = \frac{1}{\lambda}\int_0^s \mathrm{d}s'\,\sigma_\mathrm{s}(\cos\Theta, E) \tag{15.22}$$

is the angular distribution of a single-scattering event with probability $\lambda e^{-\lambda}$ taking into account energy loss, and

$$g_l = \frac{1}{\lambda}\int_0^s \mathrm{d}s' \int_0^\pi \mathrm{d}(\cos\Theta)\,\sigma_\mathrm{s}(\cos\Theta, E)P_l(\cos\Theta)\ , \tag{15.23}$$

which is related to the κ_l defined in Eq. 15.8.

The general from of Eq. 15.21 was suggested by Berger and Wang [BW89] as a way of reducing some of the singularity in Eq. 15.11 to make the summation for large-l tractable.

This approach has some moderate success for Class I pre-calculations but Class II algorithms must still sample "on-the-fly". Therefore, we have adopted an alternative approach.

This approach is based on a similar analysis of the small-angle multiple-scattering problem [Bie94]. Consider the part of Eq. 15.20 that describes two or more scatterings. Defining the notation

$$\psi^{(2+)}(\mu, s) = \sum_l (l + 1/2) P_l(\mu) \frac{e^{-\lambda g_l} - 1 - \lambda g_l}{e^{-\lambda} - 1 - \lambda} \ , \tag{15.24}$$

where $\mu = \cos\Theta$. The change of variables,

$$u = (1 + a)\left(1 - \frac{2a}{1 - \mu + 2a}\right) \tag{15.25}$$

allows us to write an alternate form of $\psi^{(2+)}(\mu, s)$, namely

$$q^{(2+)}(u, s)\mathrm{d}u = \psi^{(2+)}(\mu, s)\mathrm{d}\mu \ , \tag{15.26}$$

where for the moment, a is an arbitrary parameter.

The motivation for this transformation is quite subtle. The magnitude of the derivative of u with respect to μ is:

$$\mathrm{d}u = (1 + a)\left(1 - \frac{2a}{1 - \mu + 2a}\right) \ , \tag{15.27}$$

which resembles a screened Rutherford cross section with an arbitrary screening angle, a. As discovered in the small-angle study, most of the shape of the multiple-scattering distribution, which is peaked strongly in the forward direction for the usual case of small screening angles, resembles a screened Rutherford cross section with some effective width. The "effective screening" angle a can then be fixed by th requirement that $q^{(2+)}(u, s)$ be as flat as possible for all angles and all transport distances. The procedure is described elsewhere. It suffices to say that the $q^{(2+)}$-surfaces produced, starting with a screened Rutherford cross section employing the Molière screening angle [Mol47] along with Mott [Mot29, Mot32] that includes spin and relativistic corrections [Mot29, Mot32], are flat enough so that a linear interpolation table that is accurate to within 0.2% can be represented in a few hundred kB of data for 100 atomic elements suitable for applications from 1 keV upwards[3].

15.3 Longitudinal and lateral distributions

In this section we consider longitudinal and lateral transport components of Monte Carlo sub-step. Although the transport scheme represented by Eq. 15.18 has been shown to yield results correct to $\mathrm{O}(\Delta s)$, it can be shown that all the moments represented by Eqs. 15.13–15.17 are not correct. Thus, even average penetration distances and lateral diffusion are not

[3]We are grateful to Dr Stephen Seltzer for providing the Mott cross section data.

accounted for correctly. For most applications, electrons scatter for many elastic and inelastic scatterings before tallying some result. After many scatterings, the only information that really matters are the first few moments. There are, of course exceptions, the most important one being low energy electron backscatter. In the application, single and plural events can lead to backscatter from a foil. The "boundary-crossing algorithm" discussed previously may come to the rescue, however. This is because electrons must penetrate using single-scattering methods to a skin-depth of several mean-free-path distances before the condensed history algorithm is allowed to take over. If single and plural scattering from within the skin-depth is contributing in a significant way to the backscatter events, then this will automatically be accounted for.

We now describe a transport algorithm that gives exactly the Lewis moments, $\langle z \rangle$, $\langle z \cos\Theta \rangle$, $\langle z^2 \rangle$, and $\langle x^2 + y^2 \rangle$ with only a little more computational effort[4].

We create the ansatz:

$$\begin{aligned} \Delta x/s &= [\beta(s) - \delta_{\parallel}(s,\xi_x)] \sin\Theta \cos[\Phi - \delta_{\phi}(s,\xi_{\phi})] + \delta_{\perp}(s,\xi_x) \\ \Delta y/s &= [\beta(s) - \delta_{\parallel}(s,\xi_x)] \sin\Theta \sin[\Phi - \delta_{\phi}(s,\xi_{\phi})] + \delta_{\perp}(s,\xi_y) \\ \Delta z/s &= [\beta(s) - \delta_{\parallel}(s,\xi_z)] \cos\Theta + [\alpha(s) - \delta_{\parallel}(s,\xi_x)] \ , \end{aligned} \tag{15.28}$$

where $\delta_{\perp}$, $\delta_{\parallel}$ and δ_{ϕ} are transverse, longitudinal and azimuthal straggling functions and ξ_i is a uniform random variable between 0 and 1. The lateral and longitudinal straggling functions have the property that their average is exactly zero, *i.e.* $\int_0^1 \mathrm{d}\xi\, \delta_{\perp}(s,\xi) = 0$ and $\int_0^1 \mathrm{d}\xi\, \delta_{\parallel}(s,\xi) = 0$ while the azimuthal straggling function's average value represents the average angle between the direction of motion and the azimuthal component of the straggling function [Kaw96a]. It also has a straggling component. This function has been determined by single-scattering calculations [Kaw96a]. The functions $\alpha(s)$ and $\beta(s)$ can be found by insisting that $\langle z \rangle$ and $\langle z \cos\Theta \rangle$ comply with $\langle z \rangle$ in Eq. 15.13 and with $\langle z \cos\Theta \rangle$ in Eq. 15.14. The values of $\int_0^1 \mathrm{d}\xi\, \delta_{\perp}^2(s,\xi)$ and $\int_0^1 \mathrm{d}\xi\, \delta_{\parallel}^2(s,\xi)$ can be determined by forcing agreement with $\langle z^2 \rangle$, and $\langle x^2 + y^2 \rangle$. It should be remarked that the shape of the straggling functions is not determined by this approach. We can derive more information about them by calculating higher Lewis moments. This will lead to information about $\int_0^1 \mathrm{d}\xi\, \delta_{\perp}^n(s,\xi)$ and $\int_0^1 \mathrm{d}\xi\, \delta_{\parallel}^n(s,\xi)$, where $n > 2$. Since we do not know the exact shape of the straggling functions, we have to guess. Small-angle theory suggests Gaussian's for the lateral straggling functions. This work remains to be done. The use of the previously-computed azimuthal straggling function, should guarantee compliance with $\langle x \sin\Theta \cos\Phi \rangle$ and $\langle y \sin\Theta \sin\Phi \rangle$.

Before ending this section, we make a few remarks on the computational efficiency of this new method. The most computationally intensive part of Eq. 15.28 is sampling the multiple-scattering distribution, which is required by any method. The straggling functions can be

[4]It is very important remark that more advanced methods have to be computationally efficient. It is pointless to develop complicated calculational schemes that cost more to execute than simply turning down the step-size to obtain the same degree of accuracy!

pre-calculated and put into interpolation tables, a task no more difficult than the multiple-scattering table described in the previous section. Alternatively, since the shape of the distributions is arbitrary, simple forms may be used and sampling these distributions may be very rapid.

One possible criticism of this approach is that it is bound to produce the occasional unphysical result of the form $x^2 + y^2 + z^s > s^2$. It is anticipated that this type of event will be rare, and some indication of this has been given by Berger [Ber63], who first suggest Gaussian straggling terms for the lateral component. Another criticism is that the ansatz in Eq. 15.28 is not general enough. Indeed, although moments of the type $\langle z^n \rangle$ can be used to determine $\int_0^1 \mathrm{d}\xi\, \delta_{\parallel}^n(s,\xi)$, they will likely be in conflict with higher order moments of the sort $\langle z^n \cos^m \Theta \rangle$. Actually, this criticism is coupled directly to the previous one and results from our incomplete understanding of the solution to the complete transport problem. Further research along these lines, such as the Fokker-Planck solution to this problem, while approximate will shed more insight on the general transport solution. However, it is also likely that Eq. 15.28 represents a significant advance in condensed history methods and may provide true step-size independence for a large class of electron transport problems.

15.4 The future of condensed history algorithms

We conclude with some comments on the future of condensed history algorithms to place its research in some sort of larger perspective. We investigate briefly two scenarios that are pointed to by present computer hardware developments. *Will condensed history continue to play a role when computers get much faster?* and *Will analog-based condensation techniques ever replace our analytic-based ones?*.

Will condensed history continue to play a role when computers get much faster?

The other was of asking this question is: *Will analog Monte Carlo techniques replace condensed history methods for most future applications?*

Depending on the application, condensed history techniques "outrun" single-scattering calculations by a factor 10^3—10^5. Computing power per unit cost increases by approximately a factor of 2 every year. This means that an application that runs today with condensed history calculations can be done in the same amount of time by analog methods in about 10–17 years!

The answer to this is that the problems usually expand in complexity as the technology to address them advances. In the next decade or two we will not be asking the same questions! The questions will be more complex and the simpler, cruder method of condensed history, whatever it evolves to in that time, will still have an important role to play.

A perfect example of this is radiotherapy treatment planning calculations. Presently, condensed history techniques are not used because it takes a few hours to perform on a workstation-

class computer. Software and hardware technology may reduce this to seconds in about 5 years, making it feasible for routine use. In a few more years, calculation times will be microseconds and Monte Carlo will be used in all phases of treatment planning, even the most sophisticated such as inverse planning and scan-plan-treat single pass tomotherapy machines.

Condensed history gets this answer to sufficient accuracy and medical physics will not resort to single-scattering methods that take 10^3—10^5 longer to execute for marginal (and and largely unnecessary) gain in accuracy. Once calculation error has been reduced to about 2% or so, its contribution to the overall error of treatment delivery will be negligible.

Will analog-based condensation techniques ever replace our analytic-based ones?

One approach to addressing the problem of slow execution for single-scattering Monte Carlo is to pre-compute electron single-scattering histories and tally the emergence of particles from macroscopic objects of various shapes, depending on the application. Then one transports these objects in the application rather than electrons! Ballinger *et. al.* [BRM92] used hemispheres as his intended application was primarily low-energy backscatter from foils. Ballinger *et. al.* did their calculations within the hemispheres almost completely in analog mode, for both elastic and inelastic events.

Neuenschwander and Born [NB92] and later Neuenschwander *et. al.* [Nel95] used EGS4 [NHR85, BHNR94] condensed history methods for pre-calculation in spheres for the intended application of transport within radiotherapy targets (CT-based images) and realized a speed increase of about 11 over condensed history. Svatos *et. al.* [SBN$^+$95] is following up on this work by using analog methods.

Since these "analog-based condensation" techniques play a role in specialized applications it begs the question whether or not these techniques can play a more general role. To answer this, consider that we are seeking the general solution to the problem: given an electron starting at the origin directed along the z-axis for a set of energies E_n, what is the complete description of the "phase space" of particles emerging from a set spheres[5] of radii r_n? That is, what is $\psi(\vec{x}, \vec{\Omega}, E, s, q; E_n, r_n)$, where $\vec{x}$ is the final position on the sphere, $\vec{\Omega}$ is the direction at the exit point of the sphere, E is the exit energy, s is the total pathlength, q is the charge (3 possible values in our model, electrons, positrons or photons), E_n is the starting energy, and r_n is the radius of the sphere. Now, imagine that we require n-points to fit some input or output phase-space variable (*e.g.* 100 different values of E) and that we must provide storage for N decades of input energy. (The input and output energies would likely be tabulated on a logarithmic mesh.) The result is that one would require $3Nn^8$ real words of data to store the results of the general problem!

To make the example more concrete, imagine that we wish to store 9 decades in input energy (from, say, 1 keV to 100 TeV) and set $n = 100$. This would require 1.2 exabytes (1.2×10^{18})

[5]We will use this geometry as an example. A set of spheres is necessary so that geometry-adaptive techniques may be employed.

bytes of information. Estimating current on-line storage capability at about 10 terabytes/m^3, the required storage would be 1.2×10^5 m^3, or a cube about 50 m on a side. This class of solution would require storage densities of the order 10^2–10^3 greater than current technology, something for the distant future, perhaps in 50 years or so?

However, this solution really reflects a paucity of clever ideas. In a previous section we have already seen how multiple-scattering angles can be represented compactly. It is likely that further research may give us more insight into how to represent the data to the entire problem in a compact way. It may turn out that the future of this class of Monte Carlo calculations may be with pre-computed distributions. However, condensed history research will provide the most sensible way to *interpolate* the data. The better the interpolation scheme, the more compact the data will be. This may be the surviving contribution of condensed history research in the distant future.

Bibliography

[AMB93] P. Andreo, J. Medin, and A. F. Bielajew. Constraints on the multiple scattering theory of Molière in Monte Carlo simulations of the transport of charged particles. *Med. Phys.*, 20:1315 – 1325, 1993.

[Ber63] M. J. Berger. Monte Carlo Calculation of the penetration and diffusion of fast charged particles. *Methods in Comput. Phys.*, 1:135 – 215, 1963.

[Bet53] H. A. Bethe. Molière's theory of multiple scattering. *Phys. Rev.*, 89:1256 – 1266, 1953.

[BHNR94] A. F. Bielajew, H. Hirayama, W. R. Nelson, and D. W. O. Rogers. History, overview and recent improvements of EGS4. *National Research Council of Canada Report PIRS-0436*, 1994.

[Bie94] A. F. Bielajew. Plural and multiple small-angle scattering from a screened Rutherford cross section. *Nucl. Inst. and Meth.*, B86:257 – 269, 1994.

[Bie95] A. F. Bielajew. HOWFAR and HOWNEAR: Geometry Modeling for Monte Carlo Particle Transport. *National Research Council of Canada Report PIRS-0341*, 1995.

[Bie96] A. F. Bielajew. A hybrid multiple-scattering theory for electron-transport Monte Carlo calculations. *Nucl. Inst. and Meth.*, B111:195 – 208, 1996.

[Bot21] W. Bothe. Das allgemeine Fehlergesetz, die Schwankungen der Feldstärke in einem Dielektrikum und die Zerstreuung der α-Strahlen. *Z. für Physik*, 5:63 – 69, 1921.

[BR86] A. F. Bielajew and D. W. O. Rogers. PRESTA: The Parameter Reduced Electron-Step Transport Algorithm for electron Monte Carlo transport. *National Research Council of Canada Report PIRS-0042*, 1986.

[BR87] A. F. Bielajew and D. W. O. Rogers. PRESTA: The Parameter Reduced Electron-Step Transport Algorithm for electron Monte Carlo transport. *Nuclear Instruments and Methods*, B18:165 – 181, 1987.

[Bri86] J. Briesmeister. MCNP—A general purpose Monte Carlo code for neutron and photon transport, Version 3A. *Los Alamos National Laboratory Report LA-7396-M (Los Alamos, NM)*, 1986.

[Bri93] J. F. Briesmeister. MCNP—A general Monte Carlo N-particle transport code. *Los Alamos National Laboratory Report LA-12625-M (Los Alamos, NM)*, 1993.

[BRM92] C. T. Ballinger, J. A. Rathkopf, and W. R. Martin. The response history Monte Carlo method for electron transport. *Nucl. Sci. Eng.*, 112:283 – 295, 1992.

[BW89] M. J. Berger and R. Wang. Multiple-scattering angular deflections and energy-loss straggling. In T.M. Jenkins, W.R. Nelson, A. Rindi, A.E. Nahum, and D.W.O. Rogers, editors, *Monte Carlo Transport of Electrons and Photons*, pages 21 – 56. Plenum Press, New York, 1989.

[FS95] B. J. Foote and V. G. Smyth. The modeling of electron multiple-scattering in EGS4/PRESTA and its effect on ionization-chamber response. *Nucl. Inst. and Meth.*, B100:22 – 30, 1995.

[GS40a] S. A. Goudsmit and J. L. Saunderson. Multiple scattering of electrons. *Phys. Rev.*, 57:24 – 29, 1940.

[GS40b] S. A. Goudsmit and J. L. Saunderson. Multiple scattering of electrons. II. *Phys. Rev.*, 58:36 – 42, 1940.

[HKM+92] J. A. Halbleib, R. P. Kensek, T. A. Mehlhorn, G. D. Valdez, S. M. Seltzer, and M. J. Berger. ITS Version 3.0: The Integrated TIGER Series of coupled electron/photon Monte Carlo transport codes. *Sandia report SAND91-1634*, 1992.

[Kaw96a] I. Kawrakow. Electron transport: longitudinal and lateral correlation algorithm. *Nuclear Instruments and Methods*, B114:307 – 326, 1996.

[Kaw96b] I. Kawrakow. Electron transport: multiple and plural scattering. *Nuclear Instruments and Methods*, B108:23 – 34, 1996.

[KB98] I. Kawrakow and A. F. Bielajew. On the representation of electron multiple elastic-scattering distributions for Monte Carlo calculations. *Nuclear Instruments and Methods*, B134:325 – 336, 1998.

[Lar92] E. W. Larsen. A theoretical derivation of the condensed history algorithm. *Ann. Nucl. Energy*, 19:701 – 714, 1992.

[Lew50] H. W. Lewis. Multiple scattering in an infinite medium. *Phys. Rev.*, 78:526 – 529, 1950.

[Mol47] G. Z. Molière. Theorie der Streuung schneller geladener Teilchen. I. Einzelstreuung am abgeschirmten Coulomb-Field. *Z. Naturforsch*, 2a:133 – 145, 1947.

[Mol48] G. Z. Molière. Theorie der Streuung schneller geladener Teilchen. II. Mehrfach- und Vielfachstreuung. *Z. Naturforsch*, 3a:78 – 97, 1948.

[Mot29] N. F. Mott. . *Proc. Royal Society London*, A124:425, 1929.

[Mot32] N. F. Mott. . *Proc. Royal Society London*, A135:429, 1932.

[NB92] H. Neuenschwander and E. J. Born. A Macro Monte Carlo method for electron beam dose calculations. *Phys. Med. Biol.*, 37:107 – 125, 1992.

[Nel95] W. R. Nelson. private communication. *(conversation with A.F. Bielajew)*, 1995.

[NHR85] W. R. Nelson, H. Hirayama, and D. W. O. Rogers. The EGS4 Code System. Report SLAC–265, Stanford Linear Accelerator Center, Stanford, Calif, 1985.

[Rog84] D. W. O. Rogers. Low energy electron transport with EGS. *Nucl. Inst. Meth.*, 227:535 – 548, 1984.

[Rog93] D. W. O. Rogers. How accurately can EGS4/PRESTA calculate ion chamber response? *Medical Physics*, 20:319 – 323, 1993.

[SBN+95] M. M. Svatos, C. T. Ballinger, H. Neuenschwander, T. R. Mackie, W. P. Chandler, C. L. Hartmann-Siantar, J. A. Rathkopf, and P. J. Reckwerdt. Electron transport in radiotherapy using local-to-global Monte Carlo. *In "Proceedings of the International Conference on Mathematics and Computations, Reactor Physics, and Environmental Analyses" (American Nuclear Society Press, La Grange Park, Illinois, U.S.A.)*, pages 154 – 161, 1995.

[Sel89] S. M. Seltzer. An overview of ETRAN Monte Carlo methods. In T.M. Jenkins, W.R. Nelson, A. Rindi, A.E. Nahum, and D.W.O. Rogers, editors, *Monte Carlo Transport of Electrons and Photons*, pages 153 – 182. Plenum Press, New York, 1989.

[Sel91] S. M. Seltzer. Electron-photon Monte Carlo calculations: the ETRAN code. *Int'l J of Appl. Radiation and Isotopes*, 42:917 – 941, 1991.

[Wen22] G. Wentzel. Zur theorie der streuung von β-strahlen. *Ann. Physik*, 69:335 – 368, 1922.

[Win87] K. B. Winterbon. Finite-angle multiple scattering. *Nuclear Instruments and Methods*, B21:1 – 7, 1987.